

# Enhanced vortex pinning by a composite antidot lattice in a superconducting Pb film

A. V. Silhanek,<sup>1\*</sup> L. Van Look,<sup>2</sup> R. Jonckheere,<sup>2</sup> B. Y. Zhu,<sup>1†</sup> S. Raedts,<sup>1</sup> and V. V. Moshchalkov<sup>1</sup>

<sup>1</sup>*Nanoscale Superconductivity and Magnetism Group,  
Laboratory for Solid State Physics and Magnetism K. U. Leuven  
Celestijnenlaan 200 D, B-3001 Leuven, Belgium. and*

<sup>2</sup>*IMEC vzw, Kapeldreef 75, B-3001 Leuven, Belgium.*

(Dated: June 24, 2018)

The use of artificial defects is known to enhance the superconducting critical parameters of thin films. In the case of conventional superconductors, regular arrays of submicron holes (antidots) substantially increase the critical temperature  $T_c(H)$  and critical current  $I_c(H)$  for all fields. Using electrical transport measurements, we study the effect of placing an additional small antidot in the unit cell of the array. This composite antidot lattice consists of two interpenetrating antidot square arrays with a different antidot size and the same lattice period. The smaller antidots are located exactly at the centers of the cells of the array of large antidots. We show that the composite antidot lattice can trap a higher number of flux quanta per unit cell inside the antidots, compared to a reference antidot film without the additional small antidots in the center of the cells. As a consequence, the field range in which an enhanced critical current is observed is considerably expanded. Finally, the possible stable vortex lattice patterns at several matching fields are determined by molecular dynamics simulations.

## I. INTRODUCTION

During the last decade, compelling evidence has shown that the introduction of an array of micro-holes (antidots) in a superconducting film has a profound influence on both the critical current<sup>1,2</sup>  $I_c(H)$  and the critical temperature<sup>3,4</sup>  $T_c(H)$ . Typically, at temperatures used for transport measurements, the antidots are able to trap only one flux quantum  $\Phi_0$  before saturation sets in. In this case, after the first matching field  $H_1$ , interstitial vortices appear in the sample, creating a “composite vortex lattice”, where part of the vortices is strongly pinned at the antidots and the rest occupies interstitial positions between the antidots.<sup>2</sup> Due to their higher mobility, the presence of interstitial vortices lowers the critical current  $I_c(H)$  significantly and broadens the  $R(T)$  transition.

In this work, we study a *composite antidot array*, consisting of two interpenetrating square lattices with the same period  $d = 1.5 \mu\text{m}$ , but different antidot size ( $a_1 = 0.55 \mu\text{m}$  and  $a_2 = 0.25 \mu\text{m}$ ). The two sublattices are shifted with respect to each other by half a unit cell along  $x$ - and  $y$ -directions, so that the small antidot is placed in the center of the unit cell of the lattice of large antidots (see Fig. 1). This arrangement of antidots corresponds to the vortex lattice configuration at the second matching field in a sample with a single square array of antidots with  $n_s = 1$ . The purpose of this experiment is to enlarge the field range where an enhanced critical current  $I_c(H)$  is observed, by having efficient pinning sites exactly at the locations where the interstitial vortices would appear if the smaller antidots were not

present.

This paper is organized as follows. In the next section we present some details concerning the sample preparation and characterization. In section III we study the phase boundary  $T_c(H)$  which allows us to identify the different vortex configurations. Section IV is devoted to the flux pinning properties of this composite array of holes by measuring the critical current as a function of field and temperature. We show that a composite antidot lattice considerably increases the critical current at high fields. This effect results from the fact that for  $H > H_2$  the saturated small holes force the incoming vortices to occupy the big antidots. This situation persists until  $H = H_4$  where the big antidots saturate and interstitial vortices form a more complex pattern. Finally, in Section V we determine the most stable vortex patterns by means of molecular dynamics simulations.

## II. SAMPLE PREPARATION AND CHARACTERIZATION

The used sample is a 50 nm-thick Pb film with a composite antidot lattice. The results obtained with this sample are directly contrasted with those measured on a reference antidot sample without the small holes, i.e.  $a_1 = 0.5 \mu\text{m}$  and  $a_2 = 0 \mu\text{m}$ . In both cases, the bridge made for transport measurements (see Fig. 1(a)) has a width of  $300 \mu\text{m}$  and a voltage contact separation of 2 mm. The unit cell of the composite antidot array is shown schematically in Fig. 1(b). The procedures followed to grow the samples are described in Ref.[5]. The transport measurements were carried out in a commercial PPMS-Quantum Design device with a temperature stability better than 0.5 mK. All measurements were performed with the field  $\mathbf{H}$  applied perpendicular to the surface of the film. The critical temperature  $T_{c0} = 7.207 \text{ K}$

\*present address: MST-NHMFL, MS E536, Los Alamos National Laboratory, Los Alamos, NM 87544, USA.

†National Laboratory for Superconductivity, Institute of Physics, Chinese Academy of Sciences, Beijing 100080, China.

was determined from the resistive transition  $R(T)$  in zero field, using a criterion of 10% of the normal state resistance  $R_n$ .

FIG. 1: Layout of the Pb film with a composite array of square antidots of two different sizes. (a) Geometry of the sample showing the patterned area in dark gray. (b) Schematic presentation of a unit cell of the antidot array. (c) Atomic force micrograph of a  $5 \times 5 \mu\text{m}^2$  area of the composite antidot array. The lattice period  $d$  is  $1.5 \mu\text{m}$ , the antidot sizes are  $a_1 = 0.55 \mu\text{m}$  and  $a_2 = 0.25 \mu\text{m}$ .

Due to the lateral nanostructuring, the effective width of the sample is reduced from  $300 \mu\text{m}$  to  $140 \mu\text{m}$ . Here, we have assumed that we can model the antidot sample as a set of 200 parallel strips of width  $0.7 \mu\text{m}$  ( $= 2 \cdot 0.35 \mu\text{m}$ ). This effective width was employed to calculate the resistivity  $\rho(7.5 \text{ K}) = 5.33 \cdot 10^{-8} \Omega\text{m}$  from the resistance  $R(7.5 \text{ K}) = 15.2 \Omega$ . Using the listed value<sup>6</sup> for  $\rho\ell = 4.88 \cdot 10^{-16} \Omega\text{m}^2$ , this resistivity value gives an elastic mean free path of  $\ell = 9 \text{ nm}$ , and therefore a superconducting coherence length  $\xi(0) = 25 \text{ nm}$  (in the dirty limit). These values are noticeably smaller than those obtained for the reference antidot sample ( $\ell = 27 \text{ nm}$  and  $\xi(0) \approx 40 \text{ nm}$ ). Since in a film without antidots coevaporated with the sample containing the composite antidot was obtained  $\ell = 27 \text{ nm}$ , this difference seems to be caused by the more complex lift-off procedure due to the presence of the small holes.

Knowing the mean free path  $\ell$  and using the London penetration depth for the bulk<sup>7</sup> Pb we obtain  $\lambda(0) = 71 \text{ nm}$ . Due to the perforation, the effective penetration depth increases, and therefore  $\lambda$  should be modified according to<sup>9</sup>

$$\Lambda_a(0) = \frac{\lambda(0)}{\sqrt{1 - 2\frac{S_a}{S_t}}} = 86 \text{ nm}, \quad (1)$$

where  $S_a$  and  $S_t$  are the area of the holes and the total area per unit cell, respectively. As a result, the Ginzburg-Landau parameter  $\kappa$  amounts to  $\kappa = \frac{\Lambda(0)}{\xi(0)} = 3.4 > \frac{1}{\sqrt{2}}$ , and therefore this sample is a Type-II superconductor.<sup>10</sup>

The sample has been characterized by means of atomic force microscopy. An AFM topograph of a  $5 \times 5 \mu\text{m}^2$  area of the film containing a composite antidot lattice is shown in Fig. 1(c). The root-mean-square roughness on a  $1 \mu\text{m}^2$  area of the sample in between the antidots is  $\sigma_{RMS} = 3 \text{ nm}$ . This value is about two times larger than for the plane film and the reference sample with antidots. This difference reinforces the idea that the film with the composite antidot lattice has suffered a small degradation due to a more complicated lift-off procedure.

### III. SUPERCONDUCTING $T_c(H)$ PHASE BOUNDARY

#### A. Experimental results

We have measured the critical temperature  $T_c(H)$  as a function of field for the sample with a composite antidot lattice. The results obtained with a resistance criterion of 10 % of the normal state resistance  $R_n$  and a measuring current of  $I_{ac} = 10 \mu\text{A}$  are shown in Fig. 2, together with the phase boundary obtained for the reference antidot film. The solid line depicts the expected upper critical field boundary of a plain film with the same coherence length as the reference antidot sample according to  $H_{c2} = \Phi_0/2\pi\xi(T)^2$ . It is important to notice that the measured boundary of the reference antidot film is close to the  $H_{c3}(T)$  line corresponding to the surface nucleation of superconductivity around the holes, whereas the solid line represents the bulk superconducting transition  $H_{c2}(T)$ . As a rule, the experimentally determined critical temperature  $T_c(H)$  of a patterned sample turns out to be higher than that obtained for a plain film with the same coherence length.<sup>4</sup>

FIG. 2:  $T_c(H)$  phase boundary for the film patterned with a composite antidot array, measured with an ac current of  $I_{ac} = 10 \mu\text{A}$  and a resistance criterion of  $R_{crit} = 10\% R_n$  (filled symbols). The open symbols show the phase boundary obtained for the reference antidot sample using the same criterion. The solid line is the calculated linear  $T_c(H)$  phase boundary for a plain film with the same coherence length  $\xi(0) = 40 \text{ nm}$  as the antidot patterned film. The field axis is normalized to the first matching field  $H_1 = 9.2 \text{ G}$ . The temperature axis is normalized to  $T_{c0}$ , the transition temperature at  $H = 0$ .

Due to the presence of the antidot array, matching features appear in  $T_c(H)$  with a periodicity of  $H_1 = \Phi_0/d^2 = 9.2 \text{ G}$ , corresponding to the lattice parameter  $d = 1.5 \mu\text{m}$ . Although not all of them are very pronounced, local maxima are visible in the  $T_c(H)$  of the composite array for all integer matching fields  $H_n$  ( $n = 1, 2, \dots, 6$ ), whereas no evidence of rational matching features is observed. Thus, *the addition of the extra antidot in the center of the unit cell of the array with large antidots, leaves the matching period unchanged*. This is an important observation, since the composite antidot lattice can also be regarded as a square lattice, tilted by  $45^\circ$ , with a unit cell twice as small as that of the original lattice. If this were the periodicity felt by the vortices, the matching period would amount to  $18.4 \text{ G}$ , which is twice as large as the observed period. In that case, one would expect the local maxima at even matching fields  $H_n$  ( $n = 2, 4, \dots$ ) in Fig. 2 to be more pronounced than the ones at odd matching fields  $H_n$  ( $n = 1, 3, \dots$ ). Since this is not the case, we conclude that all these peaks correspond to integer matching fields, indicating that *the main period felt by the vortices is the period of the lattice*

with large antidots.

In order to identify the vortex patterns at the matching fields, we have plotted the  $R(T)$  transition width  $\Delta T_c(H) = T_c(R_{\text{crit}} = 97\%R_n) - T_c(R_{\text{crit}} = 0.1\%R_n)$  as a function of  $H$  in Fig. 3 (filled symbols). In this plot three different regimes can be clearly distinguished. For  $H < H_4$ , the coherence length is larger than the width of the strands thus leading to a parabolic background in the  $T_c(H)$  phase boundary. In this so-called ‘‘collective’’ regime, we observe that the  $R(T)$  transition width remains almost constant. For fields higher than  $H_4$ , an increase of the transition width can be observed, superposed with matching features at  $H_5$  and  $H_6$ . We interpret the *sudden increase in the transition width as a crossover to the regime where interstitial vortices appear in the sample*.

The interstitial regime is indicated by the gray area in Fig. 3 for the composite array. This regime ranges up to  $3.6 \xi(T) = d - a$ , i.e. up to  $\sim H_8$ , where a change in the  $\Delta T_c(H)$  slope can be observed. For higher fields, the single object regime is entered, where a linear phase boundary slightly distorted by an oscillation with period<sup>4</sup>  $H^* = \Phi_0/a_1^2 \sim 69$  G, is expected. Although the linear phase boundary is indeed observed, single object oscillations are difficult to resolve in the narrow field range investigated. For comparison, in the same figure we show  $\Delta T_c(H) = T_c(R_{\text{crit}} = 99\%R_n) - T_c(R_{\text{crit}} = 0.1\%R_n)$  for the reference antidot sample (open symbols). From this curve we can infer that if the smaller additional antidots are absent, the crossover to the interstitial regime occurs at  $H \sim 1.5 H_1$ . Therefore the presence of the additional smaller antidots has substantially delayed the appearance of interstitial vortices. From the  $\Delta T_c(H)$  curve, we thus conclude that *the total number of trapped flux quanta per unit cell of the antidot lattice is at least four*.

FIG. 3: Filled symbols: transition width  $\Delta T_c(H) = T_c(R_{\text{crit}} = 97\%R_n) - T_c(R_{\text{crit}} = 0.1\%R_n)$  of the film with a composite antidot array, measured with a current of  $I_{\text{ac}} = 10 \mu\text{A}$ . The gray box marks the ‘‘interstitial’’ regime, where the increase of  $\Delta T_c(H)$  indicates the appearance of interstitial vortices. Open symbols: transition width  $\Delta T_c(H) = T_c(R_{\text{crit}} = 99\%R_n) - T_c(R_{\text{crit}} = 0.1\%R_n)$  of the reference antidot film for  $I_{\text{ac}} = 10 \mu\text{A}$ . The thin black arrows indicate the ordinate scale for each curve.

In other words, the observed saturation number is much larger than in the reference antidot sample, where only a  $\Phi_0$ -vortex can be pinned per antidot. Even taking into account the fact that the large antidots in the composite antidot lattice are slightly larger ( $a = 0.55 \mu\text{m}$ ) than in the reference antidot sample ( $a = 0.5 \mu\text{m}$ ) and the difference in coherence length, this is still a rather surprising observation. Indeed, the addition of *one* small hole per unit cell of the antidot array leads to an unexpected *increase of the number of pinned flux quanta per unit cell from one to four*.

## B. Discussion

To determine the number of flux quanta located in the large and the small antidots of the composite antidot array, a further investigation of the  $T_c(H)$  phase boundary is needed. As explained in Ref.[4], the background of the phase boundary is parabolic as long as  $1.8 \xi(T) > d - a$  (collective regime). In a square antidot lattice, this envelope is described by<sup>11</sup>

$$T_c(H) = T_{c0} \left[ 1 - \left( \frac{\mu_0 H \xi(0) \pi (d - a)}{\sqrt{3} \Phi_0} \right)^2 \right]. \quad (2)$$

By fitting the  $T_c(H)$  data points at the integer matching fields with this formula, the effective width  $d - a$  of the strands between the antidots can be deduced.

FIG. 4:  $T_c(H)$  of the sample with a composite antidot array (open symbols). The solid line is a fit of the parabolic background (Eq. (3)) shifted in field by one matching period. This line nicely interpolates between the  $T_c(H_n)$  points at the four matching fields ( $n = 2, \dots, 5$ ).

This procedure is, of course, not *a priori* valid for a composite antidot lattice. However, part of the  $T_c(H)$  phase boundary clearly shows a parabolic background. The parabola providing the best envelope for the data points between  $H_2$  and  $H_4$  is depicted by a solid line in Fig. 4. For fields higher than  $H_5$ , the measured curve deviates from the fitted parabola, as is expected for the ‘‘interstitial’’ regime starting for fields higher than  $H_4$ . Strikingly, the fitted parabolic background turns out to be shifted by one matching period, having its maximum at  $H_1$  instead of at  $H = 0$ . By allowing this shift, the following parabolic envelope can be found for the second up to the fourth (or even fifth) matching peak, described by

$$T_c(H) = T'_{c0} \left[ 1 - \left( \frac{\mu_0 (H - H_1) \xi(0) \pi (d - a_{\text{eff}})}{\sqrt{3} \Phi_0} \right)^2 \right], \quad (3)$$

using  $T'_{c0} = 7.195$  K and an effective antidot size of  $a_{\text{eff}} = 0.72 \mu\text{m}$ . From this, we deduce that, after the second matching field  $H_2$ , *the film with a composite antidot lattice with a filled small antidot behaves as if it would have contained a single square antidot array, but with a larger antidot size ( $a_{\text{eff}} = 0.72 \mu\text{m}$ )*.

The following scenario might explain such a behavior. Up to  $H_1$ , the vortices will be attracted towards the large antidots. Between  $H_1$  and  $H_2$ , vortices begin to occupy the small antidots. Due to their size, these small antidots trap at most a single quantum vortex. They will therefore be completely saturated at  $H_2$ , creating a repulsive potential at the position of the small antidot. Fig. 5 shows a schematic evolution of the potential landscape along a diagonal of the array (see dotted line in the inset) that would be experienced by a vortex for  $H = 0$ ,

$H_1$ , and  $H_2$ . Since the large antidots pin one flux quantum, at  $H = H_1$  a surface barrier has emerged at the antidot edges. For  $H = H_2$ , the contribution to the potential of the small antidot at the center of the unit cell is strongly repulsive. When additional vortices enter the sample, they will be pushed towards the large antidots, leading to an increase of their effective saturation number. In other words, *the additional repulsive potential at the small antidots helps to increase the saturation number of the larger antidots*. Within this scenario, for  $H > H_2$ , the phase boundary  $T_c(H)$  of the composite antidot lattice with a saturated smaller antidot resembles strongly the phase boundary expected for a simple square antidot lattice, without small antidots in the center, but with a larger antidot size. Due to this larger effective size, these antidots are then able to trap more vortices. *We therefore conclude that of the four flux quanta trapped per unit cell of the composite antidot lattice, one is pinned by the small antidot, while three are pushed into the larger holes*. The net effect of the addition of the smaller hole in the antidot film, is to increase the effective pinning capacity (or effective saturation number) of the lattice with large antidots. This leads to a substantial broadening of the field range where a strong  $T_c(H)$  enhancement is observed. A similar picture was introduced by Doria and co-workers to explain the multiple trapping of vortices at high fields, as a result of the pressure exerted by the external vortices into the pinning site.<sup>8</sup>

FIG. 5: Schematic representation of the potential along a diagonal of the composite antidot array (see inset), experienced by a vortex entering the sample for  $H = 0$ ,  $H_1$ , and  $H_2$ .

The potential at  $H = H_2$ , drawn schematically in the lower panel of Fig. 5, can be seen as a checkerboard pattern with consecutively a repulsive and an attractive site. In a recent calculation, Lindquist and Riklund have modified the classical problem of a two-dimensional electron gas exposed to a magnetic field<sup>12</sup> by adding a periodic checkerboard-like on-site potential with alternating signs<sup>13</sup>. Since the lowest energy level  $E_{LL}(H)$ , found for this classical problem, corresponds to the  $T_c(H)$  phase boundary of a simple square antidot lattice in the “collective” regime, we believe that the addition of the checkerboard on-site potential in the theory corresponds to our experimental situation for the composite antidot lattice at fields higher than the second matching field ( $H > H_2$ ). These authors showed that both the integer and the rational matching features in  $E_{LL}(H)$  are smeared out in the checkerboard system. These results may explain why the matching features in  $T_c(H)$  are much weaker for  $H > H_2$ , than for  $H < H_2$  (see Fig. 4). Indeed, it is only when  $H_2$  is exceeded that the checkerboard-like pinning potential is realized experimentally.

Summarizing the results of the  $T_c(H)$  phase boundary measurements, the composite antidot lattice shows enhanced pinning, with many integer matching features appearing for fields up to  $H_6$ . The broadening of the

$R(T)$  transition after  $H_4$  indicates that at least four flux quanta can be trapped per antidot. From the shift in magnetic field of the parabolic background of  $T_c(H)$  with one matching period, we have deduced that the small antidot pins a  $\Phi_0$ -vortex, while  $3\Phi_0$ -vortices are trapped by the large antidots. The presence of the additional small antidot in the center of the unit cell has therefore led to a substantial broadening of the collective regime, or, in other words, to an increase of the effective saturation number  $n_s$  of the large antidots from one to three.

#### IV. CRITICAL CURRENT AS A FUNCTION OF FIELD

So far we have explored the normal-superconducting boundary in order to experimentally determine the extension of the different regimes given by the ratio  $\xi(T)/(d-a)$ . Now we turn to isothermal critical current measurements which allow us to study the vortex dynamics deep in the superconducting state.

The critical current as a function of field  $I_c(H)$  was measured using a 100  $\mu\text{V}$  voltage criterion for several temperatures close to  $T_c(H)$ . The results, in order of decreasing temperature, are shown in Figs. 6 and 7.

The absolute value of the critical current density at zero field for the composite antidot array amounts to  $I_{co} = I_c(H = 0) = 6.8 \cdot 10^8 \frac{\text{A}}{\text{m}^2}$  at  $T/T_{c0} = 0.974$ . This value is a factor  $\sim 3$  lower than the critical current density obtained for the reference antidot lattice, in part due to the difference in  $\lambda(0)$  and  $\xi(0)$ , which eventually determine the pinning properties. The specific geometry of the lateral nanopatterning might also influence the current distribution throughout the film, hereby also affecting the critical current  $I_{co}$ . In order to compare the pinning properties of the film with the composite antidot lattice (open symbols) and the reference antidot lattice (solid lines) measured at the same reduced temperature we have normalized the critical current by  $I_{co}$ . Notice that since the saturation number  $n_s$  is mainly determined by the coherence length<sup>14,15</sup>  $\xi(T)$  which in turn depends solely on the reduced temperature  $t = T/T_c$ , *regardless the value of the applied magnetic field*, it is enough to compare the results obtained on these samples at the same reduced temperature, without the necessity of normalizing the field.

FIG. 6: Normalized critical current at  $T/T_{c0} = 0.997$  and  $T/T_{c0} = 0.993$  of a film with a composite antidot array. The curves were measured for  $H < 0$  (open symbols) and symmetrized for clarity for  $H > 0$  (dashed line). For comparison, the solid line shows the normalized critical current  $I_c(H)/I_{c0}$  obtained for the film with the reference antidot lattice.

The  $I_c(H)/I_{c0}$  curves for the film with a composite antidot array (Figs. 6 and 7) have been measured for negative fields (open symbols) and symmetrized for  $H > 0$  for clarity (dashed lines). All curves show distinct periodic

FIG. 7: Normalized critical current at  $T/T_{c0} = 0.986$  and  $T/T_{c0} = 0.974$  of a film with a composite antidot array. The curves were measured for  $H < 0$  (open symbols) and symmetrized for clarity for  $H > 0$  (dashed line). For comparison, the solid line shows the normalized critical current  $I_c(H)/I_{c0}$  obtained for the film with the reference antidot lattice.

matching features, with a period  $H_1 = \frac{\Phi_0}{d^2} = 9.2$  G corresponding to the unit cell of the lattice with the large (or the small) antidots ( $d = 1.5 \mu\text{m}$ ). As we pointed out before, the periodicity felt by the vortices is defined by one of the interpenetrating antidot lattices of the composite array, and not by the resulting square lattice with a unit cell which is twice as small and rotated by  $45^\circ$ .

In the upper panel of Fig. 6 ( $T/T_{c0} = 0.997$ ), the  $I_c(H)/I_{c0}$  curve of the film with a composite antidot lattice shows a peak-like behavior with sharp maxima at  $H_1$ ,  $H_2$ , and  $H_3$ . This behavior is expected at temperatures sufficiently close to  $T_{c0}$ , where it is not possible to have interstitial vortices in the superconducting strands between the antidots. As we have already deduced from the shape of the  $T_c(H)$  phase boundary (Section III), interstitial vortices indeed appear in the sample only for  $T/T_{c0} \leq 0.994$ .

At a lower temperature,  $T/T_{c0} = 0.993$  (Fig. 6, lower panel), and all temperatures below that (Fig. 7), a strong enhancement of  $I_c(H)/I_{c0}$  in the film with a composite antidot lattice can be found for fields higher than the first matching field  $H_1$ , compared to the reference antidot lattice. The reason for this lies in the *ability of the composite antidot lattice to pin more flux quanta inside the antidots compared to the reference antidot array* (see Section III).

It should be noted that the field range where the film has a finite critical current, i.e. where the film remains superconducting, is considerably broader for the composite than for the reference antidot array.

The appearance and sharpness of the matching features in the  $I_c(H)/I_{c0}$  curves, are temperature dependent. At  $T/T_{c0} = 0.993$  (Fig. 6, lower panel), every integer matching peak up to  $H_6$  can be clearly seen. The maxima at  $H_1$ ,  $H_2$ , and  $H_3$  are very pronounced. At  $H_4$  and  $H_5$ , one finds cusps rather than local maxima in  $I_c(H)/I_{c0}$ . The matching feature at  $H_6$  is again peak-like. This indicates that the vortex patterns formed at  $H_4$  and  $H_5$  are less stable than the vortex configuration at  $H_6$ .

When the temperature is lowered to  $T/T_{c0} = 0.986$  (Fig. 7, upper panel), we find again sharp matching features in  $I_c(H)/I_{c0}$  at  $H_1$ ,  $H_2$  and  $H_3$ , and only very weak cusps at  $H_4$  and  $H_5$ . At  $H_6$ , the local maximum has developed into a pronounced cusp, after which a substantial change in the  $I_c(H)/I_{c0}$  slope occurs. A second smaller slope change can be found at  $H_7$ . At the lowest measured temperature,  $T/T_{c0} = 0.974$  (Fig. 7, lower panel), the only matching features left are the sharp local maxima at  $H_1$ ,  $H_2$ , and  $H_3$ , and one pronounced cusp at  $H_7$ .

FIG. 8: Suggested vortex pattern at  $H_4$ ,  $H_5$ ,  $H_6$ , and  $H_7$ . All patterns have been obtained by molecular dynamics simulations by an annealing procedure, except the one at  $H_4$ . Open circles and black dots represent pinning sites and single quantum vortices, respectively.

It appears that, at this temperature, the seventh matching field  $H_7$  plays the same role as the sixth matching field  $H_6$  at  $T/T_{c0} = 0.986$ . This fact leads us to believe that at  $T/T_{c0} = 0.974$ , *the total number of trapped flux quanta per unit cell of the composite lattice, has increased from four to five*.

It is worth to notice that the normalized critical current at the first matching field  $H_1$  reaches approximately the same value for the film with the composite and with the reference antidot lattice, except for the  $I_c(H)/I_{c0}$  curve taken at  $T/T_{c0} = 0.997$ . This fact makes the film with the reference antidot array a good candidate to compare its pinning properties with those of the composite antidot array.

## V. STABLE VORTEX PATTERNS

The periodic matching features in the  $T_c(H)$  phase boundary and in the critical current versus field curves  $I_c(H)$  demonstrate that the composite antidot lattice can stabilize commensurate vortex lattices at several magnetic fields. From the results presented in Section III, it is clear that the large antidots trap at least three flux quanta, while the smaller antidots are saturated after pinning one single quantum vortex. The vortex patterns expected in the composite antidot lattice will therefore differ from the known patterns in simple square pinning arrays.

We have performed molecular dynamics simulations to obtain the vortex patterns at the matching fields  $H_5$ ,  $H_6$ , and  $H_7$ . To model the composite vortex lattice, two interpenetrating arrays of Gaussian sites with a different radius and a different pinning force were used. This was necessary to obtain an occupation of  $3\Phi_0$ -vortices in the large pinning sites, and of one  $\Phi_0$ -vortex in the small pinning sites. By applying an annealing course, in which the temperature is lowered, starting from a high temperature and a random distribution of vortices, the most stable configuration in the given pinning potential can be found. As the temperature is lowered, the pinning sites become smaller and stronger, scaling with  $\xi(T)$  in the following way<sup>16</sup>:

$$F_p \propto F_{p0} \exp\left(-\frac{r}{\xi(T)}\right)^2, \quad (4)$$

where  $F_{p0}$  is the single site pinning force. Additionally, the vortex-vortex interaction range reduces with decreasing temperature, due to the decrease of the magnetic

penetration depth  $\lambda$ . In this type of simulation, the occupation of the pinning sites lowers with decreasing temperature. The annealing course was therefore stopped when the occupation, corresponding to our experimental situation, was achieved. Figure 8 shows the vortex configurations we suggest for  $H_4$ ,  $H_5$ ,  $H_6$ , and  $H_7$ . All patterns, except the one at  $H_4$ , are obtained from the molecular dynamics simulations. Multi-quanta vortices are represented in this model by a multiple occupation of a pinning site with (repulsive) single-quantum vortices. Since in the experiment, the pinning sites consist of real holes in the film, the vortices trapped in the same pinning site will be interpreted as multi-quanta vortices, even though they are depicted as separate single flux quantum entities in the plots. Actually, this model can be experimentally realised by an array of non fully perforated (or blind) holes. Reported results on such systems showed that blind holes are weaker pinning centers than antidots, although the overall features in both cases are very much alike.<sup>17</sup>

The vortex pattern at  $H_4$ , which is drawn schematically and was not calculated, depicts all antidots occupied with the maximum number of vortices. The large antidots trap  $3\Phi_0$ -vortices, the smaller antidots trap a  $\Phi_0$ -vortex. No interstitial vortices are present in the sample. In this case, one would expect the matching feature at  $H_4$  to be of the same kind as the one at  $H_3$ . Surprisingly, the  $I_c(H)$  curves (see e.g. Fig. 7) show only very weak matching features at  $H_4$ . However, the  $T_c(H)$  measurements and the fact that the matching peak in  $I_c(H)$  at  $H_6$  is very well defined (see discussion below), both indicate that there should be four vortices trapped per unit cell of the antidot array, leading to the suggested vortex pattern.

At  $H_5$ , there is one interstitial vortex present per unit cell of the array. It is, however, not evident where this vortex is located, since the most logical position, at the center of the unit cell, is already occupied by the filled smaller antidot. One can see a tendency of the interstitial vortices to form diagonal lines, which make zigzag traces across the sample, indicated by dashed lines in Fig. 8(b). However, the long range order which is needed to make a regular pattern, with for example straight diagonal lines or a regular zigzag, is lacking at this field. The pattern found in molecular dynamics simulations for  $H_5$  is consequently not very stable.

At  $H_6$ , a highly symmetric vortex pattern is formed. In this case, two interstitial vortices are present per unit cell, which are positioned approximately at the center of the line connecting two neighboring large antidots. Due to its high symmetry, the vortex pattern at  $H_6$  is very stable. Remarkably, the calculations for  $H_6$ , resulting in a very regular pattern, have been performed under the same conditions as the ones at  $H_5$ , where no regular pattern could be found. This is an indication of the different stability of the vortex patterns at  $H_5$  and  $H_6$ . Indeed, the matching feature at  $H_6$  in  $T_c(H)$  or  $I_c(H)/I_{c0}$  is always more pronounced than at  $H_5$  (see e.g. Figs. 3

and 7, upper panel). For the  $I_c(H)/I_{c0}$  curve measured at  $T/T_{c0} = 0.974$  (Fig. 7, lower curve), the matching cusp at  $H_7$  becomes rather sharp. We suggest that at this temperature, the large antidots are able to trap four flux quanta instead of three. In that case, the expected vortex pattern for  $H_7$  (see Fig. 8), resembles the pattern calculated for the sixth integer matching field, but with four flux quanta occupying the large antidots instead of three.

To obtain a regular pattern at  $H_7$ , with three flux quanta pinned in the large antidots, three interstitial vortices have to be accommodated per unit cell of the composite array. The calculations were not able to produce a regular vortex pattern with an occupation of three at the large pinning sites and one at the smaller pinning sites. This indicates that the stability of a vortex pattern at  $H_7$  is not very high. On the other hand, the calculation method, where  $3\Phi_0$ -vortices are represented by three separate  $\Phi_0$ -vortices, might in this case also affect the outcome of the simulation. Indeed, the cylindrical symmetry of the  $3\Phi_0$ -vortex, as it occurs in the experiment, will make it easier to obtain a regular vortex pattern.

The vortex patterns suggested in this section remain to be directly verified by using a local scanning technique, such as low temperature scanning Hall probe microscopy. Further insight into the vortex pinning and dynamics in systems with a composite pinning array may also be gained from molecular dynamics simulations.

## VI. CONCLUSIONS

We have used a composite antidot lattice, consisting of two interpenetrating antidot arrays with a different antidot size, but with the same lattice period, as a strong periodic pinning potential for the vortex lattice in a superconducting film. The shift between the two lattices is such that the smaller antidots are situated exactly at the centers of the cells of the array of large antidots. We have shown that this pinning array can stabilize the vortex lattice at several matching fields from  $H_1$  to  $H_7$ .

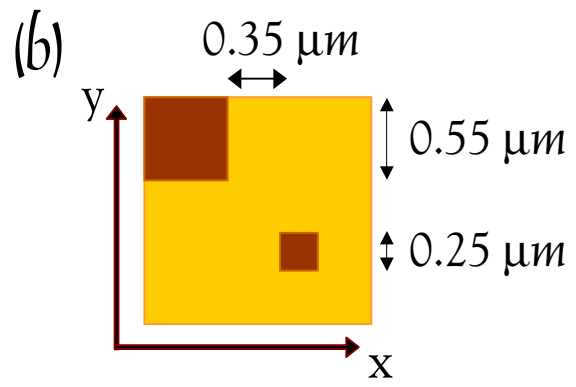
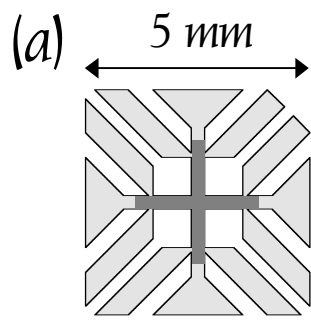
Measurements of the critical temperature  $T_c(H)$  and current  $I_c(H)/I_{c0}$  as a function of magnetic field, have demonstrated that the composite antidot lattice can trap a considerably higher amount of flux quanta per unit cell (four or five instead of one) inside the antidots, compared to a reference antidot film without the additional small antidots in the center of the unit cell. This means that the appearance of interstitial vortices in the composite antidot lattice is delayed to higher magnetic fields. The presence of the smaller antidots has therefore increased the effective saturation number of the large antidots, which has led to a considerable expansion of the field range in which an enhanced critical current is observed.

### Acknowledgments

This work was supported by the Research Fund K.U.Leuven GOA/2004/02, the Belgian Interuniversity

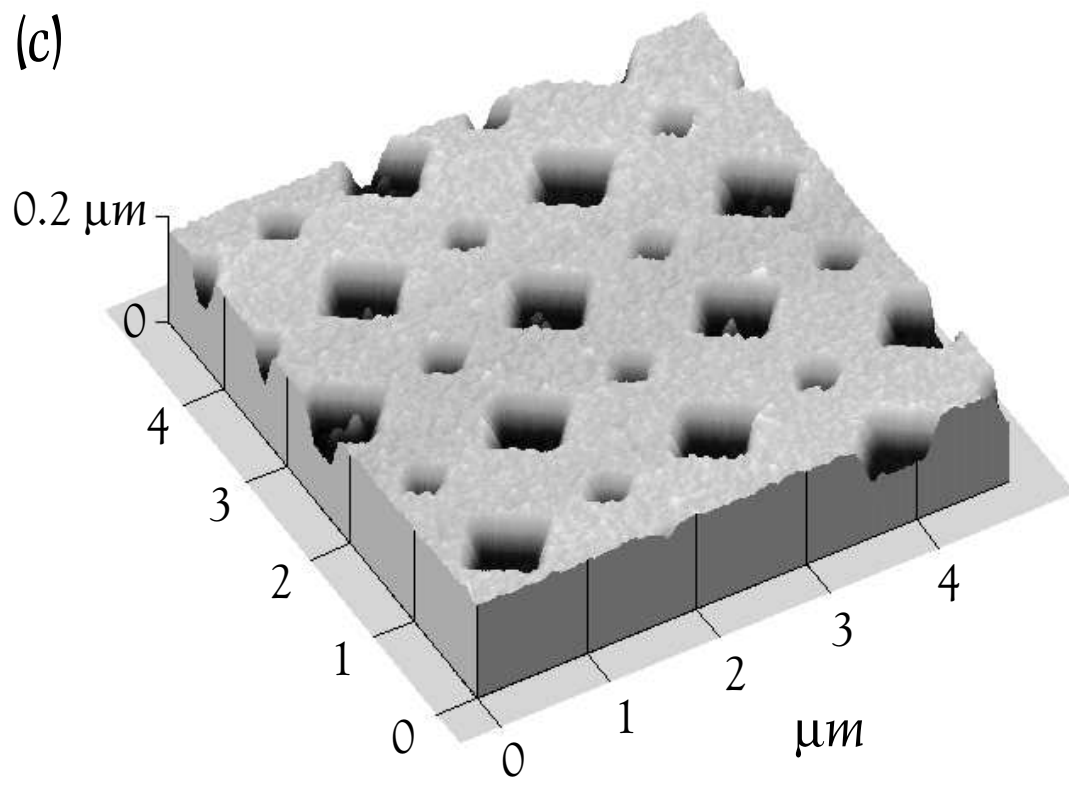
Attraction Poles (IUAP), the Fund for Scientific Research Flanders (FWO) and ESF "VORTEX" program.

- 
- <sup>1</sup> V. V. Moshchalkov, M. Baert, E. Rosseel, V. V. Metlushko, M. J. Van Bael, and Y. Bruynseraede, *Physica C* **282**, 379 (1997). V. V. Moshchalkov, M. Baert, V. V. Metlushko, E. Rosseel, M. J. Van Bael, K. Temst, and Y. Bruynseraede, *Phys. Rev. B* **57**, 3615 (1998).
- <sup>2</sup> V. Metlushko, U. Welp, G. W. Crabtree, R. Osgood, S. D. Bader, L. E. DeLong, Zhao Zhang, S. R. J. Brueck, B. Ilic, K. Chung, and P. J. Hesketh, *Phys. Rev. B* **60**, R12585 (1999).
- <sup>3</sup> U. Welp, Z. L. Xiao, J. S. Jiang, V. K. Vlasko-Vlasov, S. D. Bader, G. W. Crabtree, J. Liang, H. Chik, and J. M. Xu, *Phys. Rev. B* **66**, 212507 (2002).
- <sup>4</sup> E. Rosseel, T. Puig, M. Baert, M. J. Van Bael, V. V. Moshchalkov, and Y. Bruynseraede, *Physica C* **282**, 1567 (1997).
- <sup>5</sup> S. Raedts, A. V. Silhanek, M. J. Van Bael, and V. V. Moshchalkov, *Physica C* **404**, 298 (2004).
- <sup>6</sup> R. C. Weast (ed.), *Handbook of Chemistry and Physics* (the Chemical Rubber Co., Ohio, 1971).
- <sup>7</sup> T. P. Orlando and K. A. Delin, "Foundations of Applied Superconductivity," Addison-Wesley, Reading, MA (1991).
- <sup>8</sup> M. M. Doria and G. F. Zebende, *Phys. Rev. B* **66**, 064519 (2002).
- <sup>9</sup> A. Wahl, V. Hardy, J. Provost, Ch. Simon, A. Buzdin, *Physica C* **250**, 163 (1995).
- <sup>10</sup> Additionally to the perforation effect, the finite thickness  $\delta$  of the film also yields an increase of the effective penetration depth up to  $\Lambda = 2\lambda^2/\delta$  therefore giving rise to an even higher  $\kappa$  value. This issue has been briefly addressed in V. V. Moshchalkov, M. Baert, V. V. Metlushko, E. Rosseel, M. J. Van Bael, K. Temst, R. Jonckheere, and Y. Bruynseraede, *Phys. Rev. B* **54**, 7385 (1996).
- <sup>11</sup> B. Pannetier in "Quantum Coherence in Mesoscopic Systems", edited by B. Kramer (Plenum Press, New York, 1991), chapter 9, pp. 457-484.
- <sup>12</sup> D. R. Hofstadter, *Phys. Rev. B* **14**, 2239 (1976).
- <sup>13</sup> B. Lindquist and R. Riklund, *Phys. Rev. B* **60**, 10054 (1999).
- <sup>14</sup> G.S. Mkrtchyan and V.V. Schmidt, *Sov. Phys. JETP* **34**, 195 (1972).
- <sup>15</sup> H. Nordborg and V. M. Vinokur, *Phys. Rev. B* **62**, 12408 (2000).
- <sup>16</sup> B. Y. Zhu, L. Van Look, and V. V. Moshchalkov, B. R. Zhao, and Z. X. Zhao, *Phys. Rev. B* **64**, 012504 (2001).
- <sup>17</sup> S. Raedts, A.V. Silhanek, M. J. Van Bael, and V.V. Moshchalkov, *Phys. Rev. B* **70**, 024509 (2004).

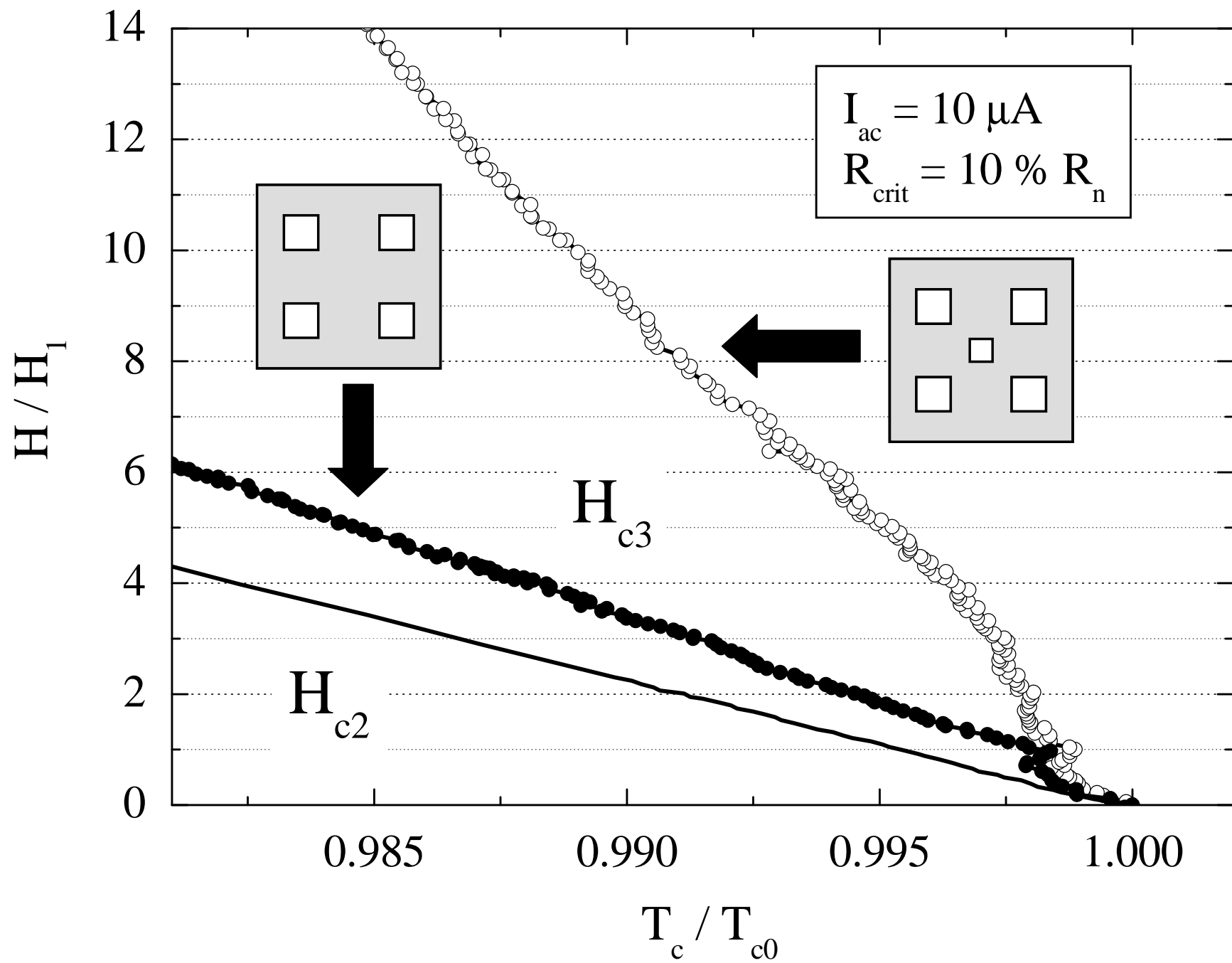


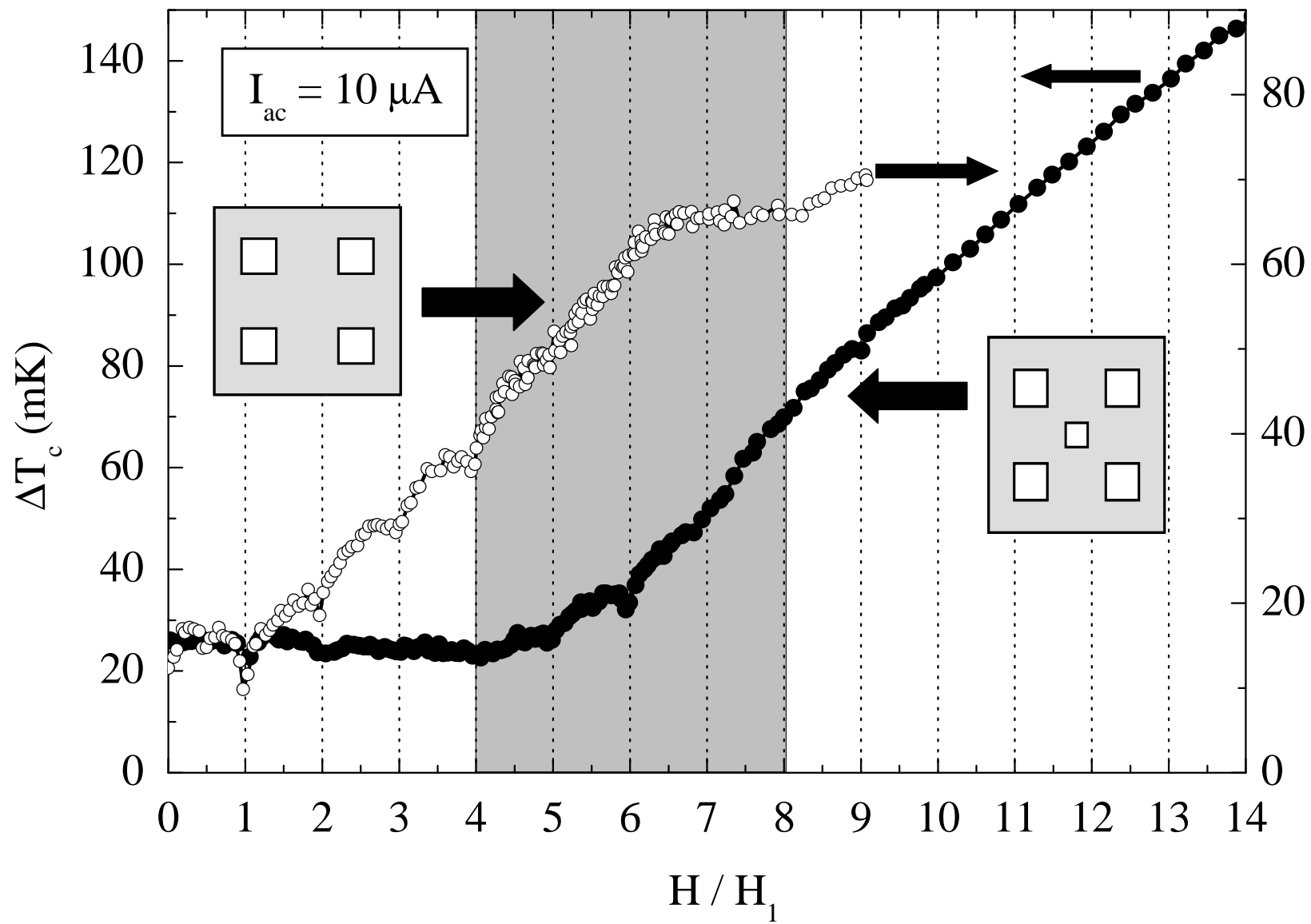
layout

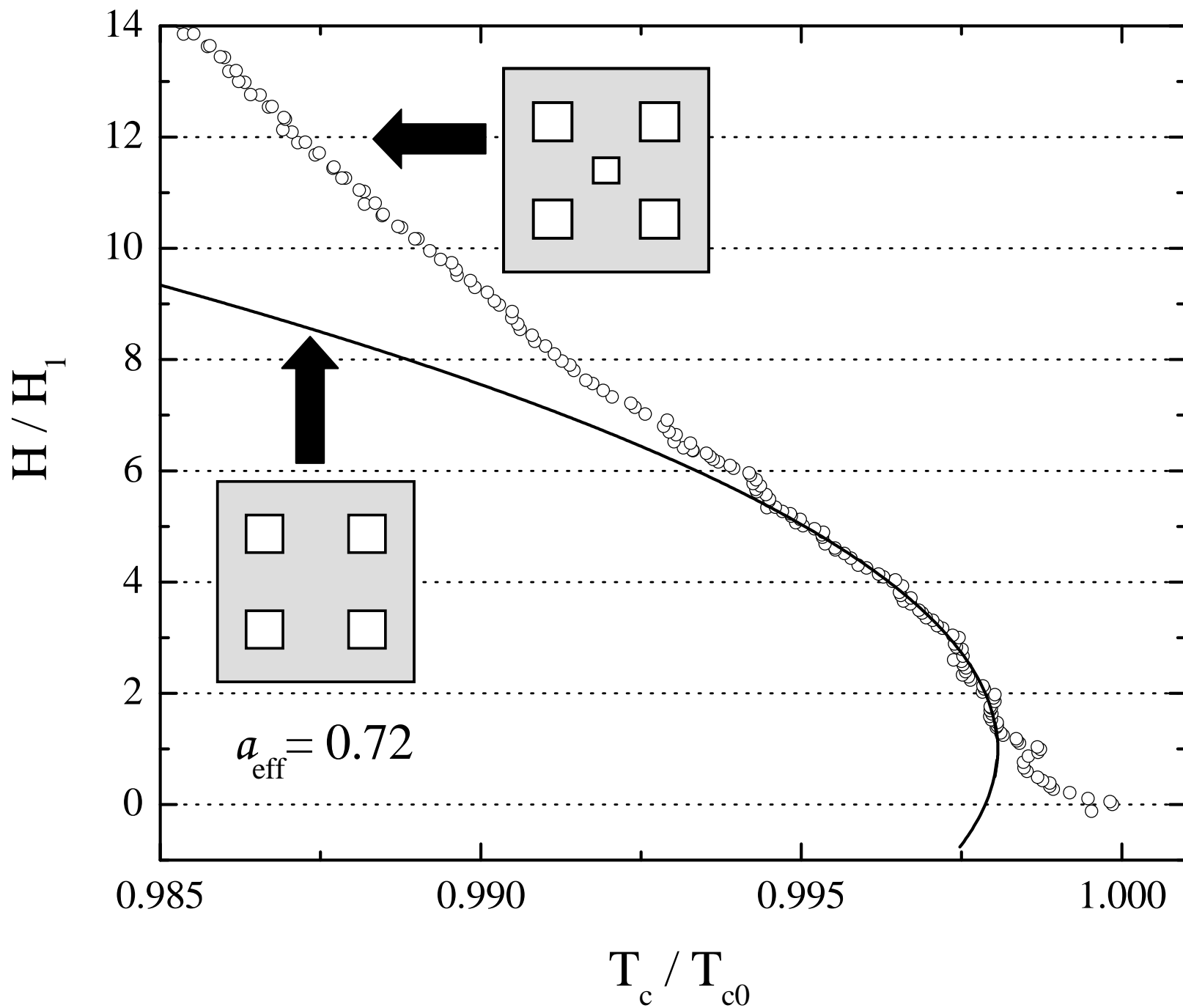
(c)

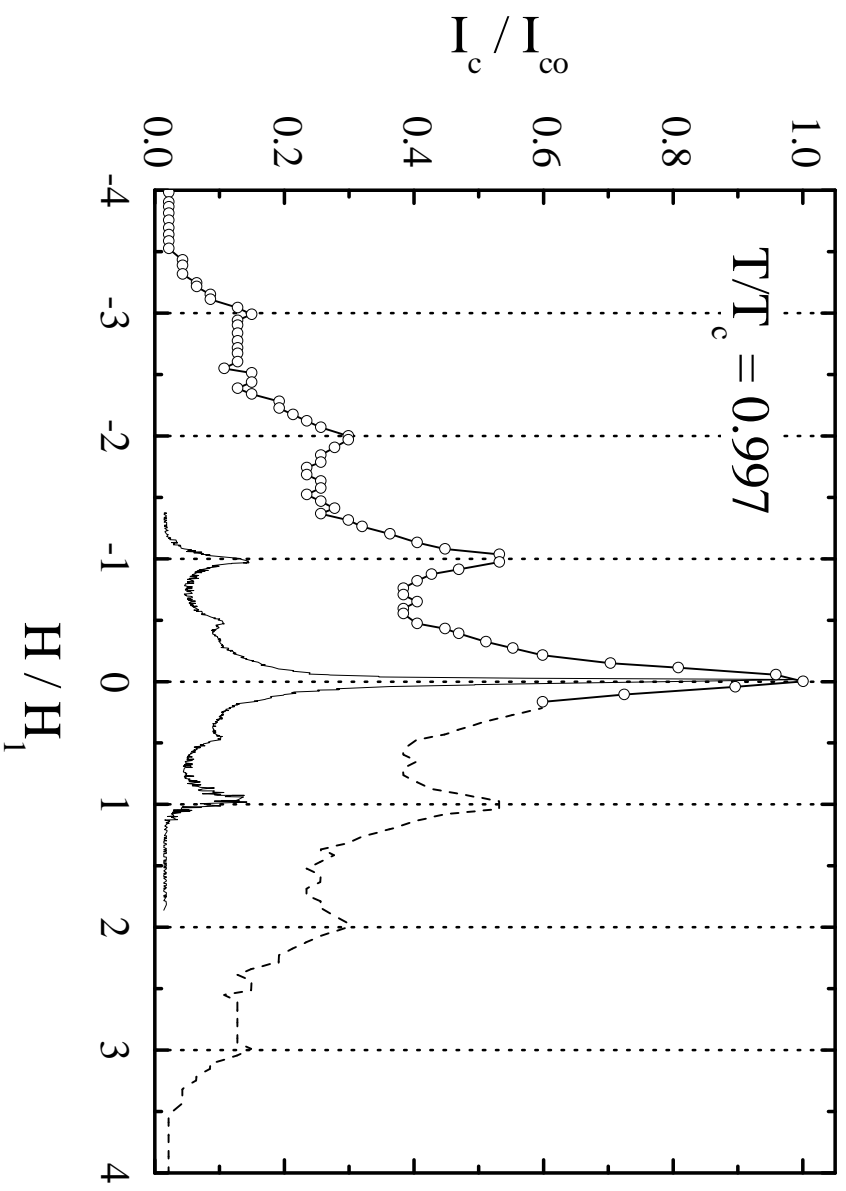


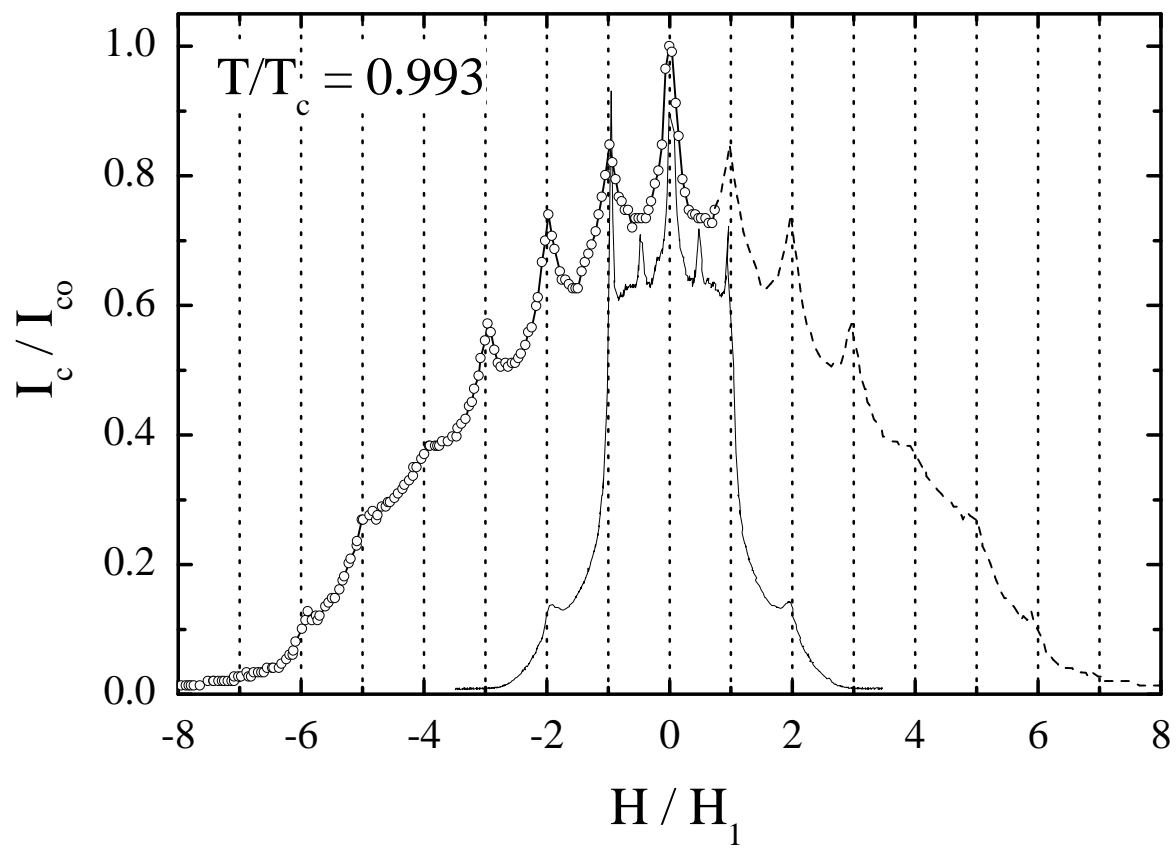
AFM

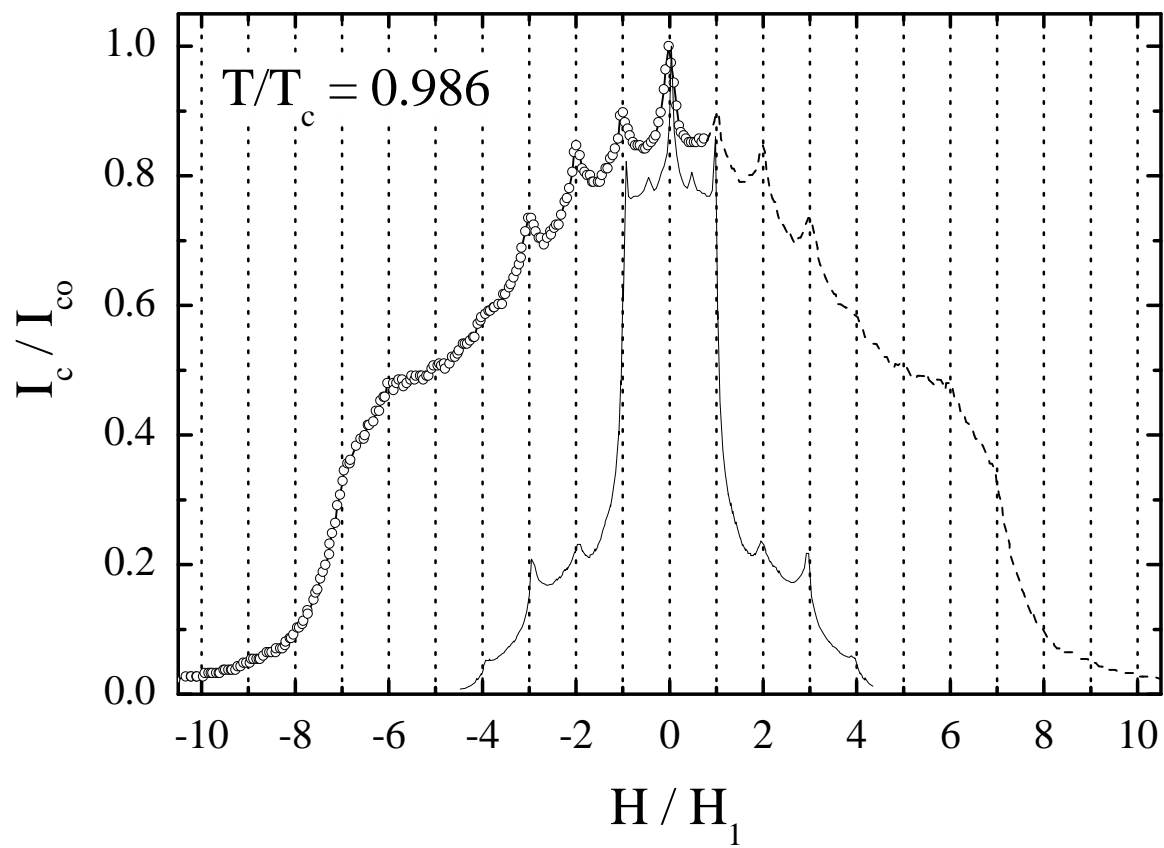


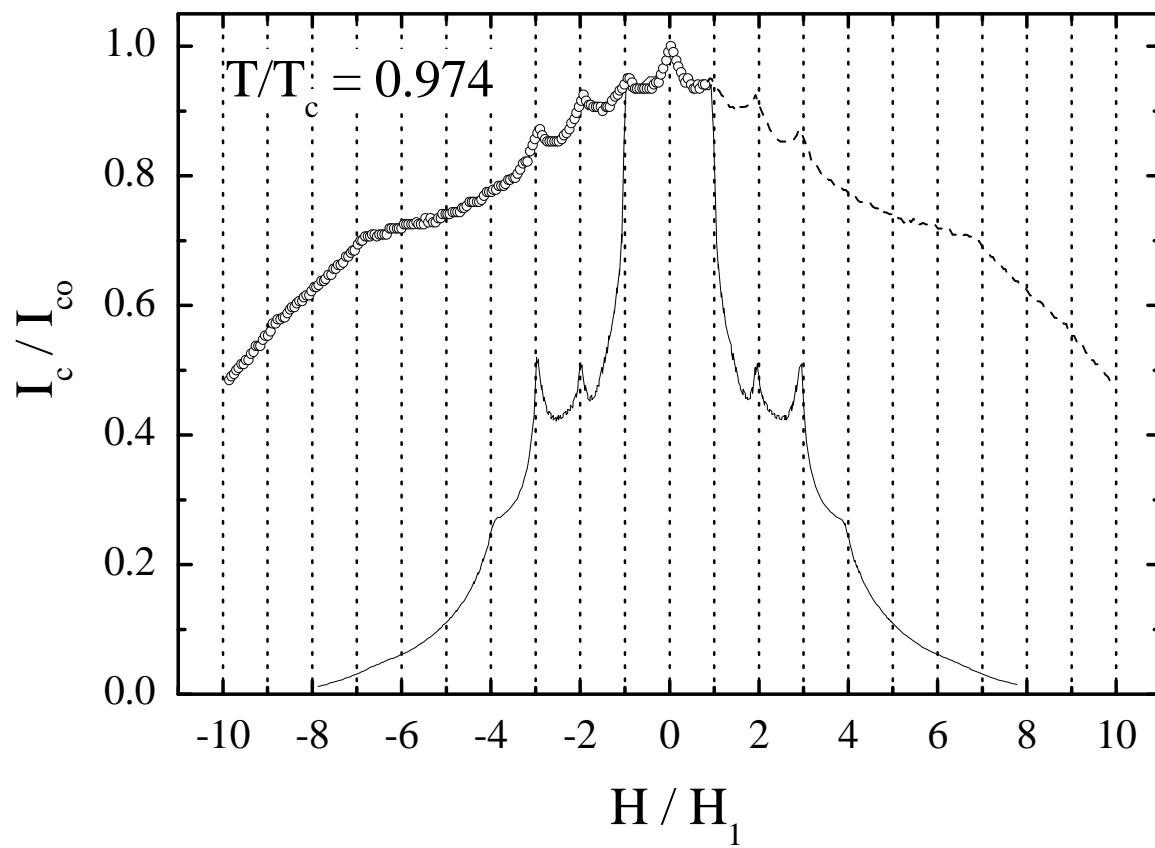






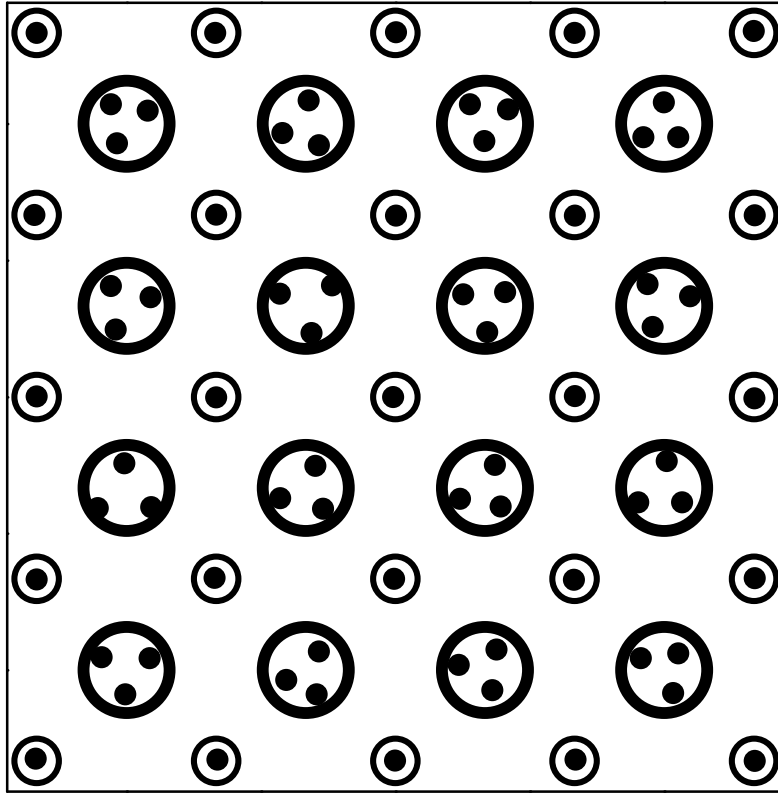






$$F_P^S = 2 * F_P^W \quad R_{\text{pin}}^S = 2 * R_{\text{pin}}^W$$

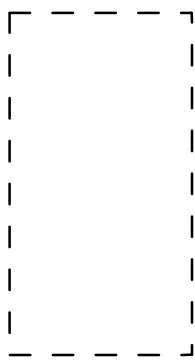
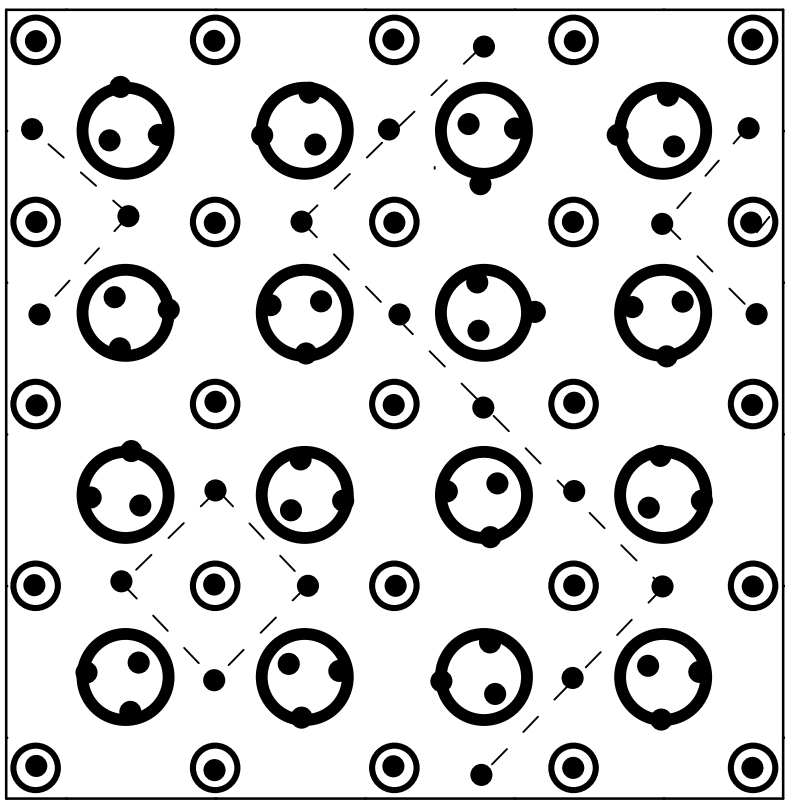
H<sub>4</sub>



$$F_P^S = 2 * F_P^W$$

$$R_{pin}^S = 2 * R_{pin}^W$$

H<sub>5</sub>



$$F_P^S = 2 * F_P^W$$

$$R_{pin}^S = 2 * R_{pin}^W$$

H<sub>6</sub>

